Ligand-Induced Fate of Embryonic Species in the Shape-Controlled Synthesis of Rhodium Nanoparticles

Adam J. Biacchi[‡] and Raymond E. Schaak*

Department of Chemistry and Materials Research Institute, The Pennsylvania State University, University Park, Pennsylvania 16802, United States. [‡]Present address: Semiconductor and Dimensional Metrology Division, National Institute of Standards and Technology (NIST), Gaithersburg, Maryland 20899, United States.

ABSTRACT

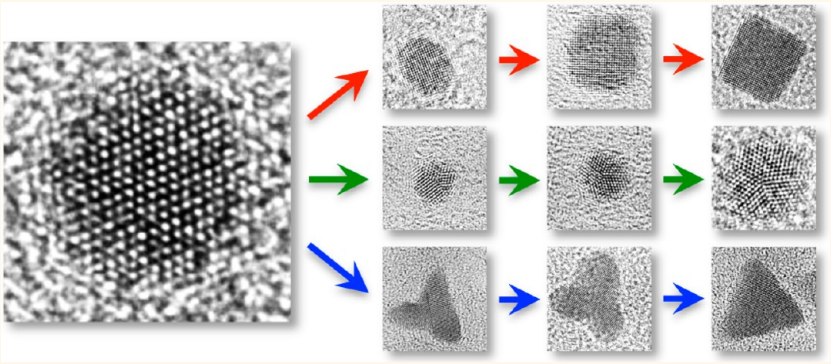

The shapes of noble metal nanoparticles directly impact their properties and applications, including in catalysis and plasmonics, and it is therefore important to understand how multiple distinct morphologies can be controllably synthesized. Solution routes offer powerful capabilities for shape-controlled nanoparticle synthesis, but the earliest stages of the reaction are difficult to interrogate experimentally and much remains unknown about how metal nanoparticle morphologies emerge and evolve. Here, we use a well-established polyol process to synthesize uniform rhodium nanoparticle cubes, icosahedra, and triangular plates using bromide, trifluoroacetate, and chloride ligands, respectively. In all of these systems, we identified rhodium clusters with diameters of 1−2 nm that form early in the reactions. The colloidally stable metal cluster intermediates served as a stock solution of embryonic species that could be transformed predictably into each type of nanoparticle morphology. The anionic ligands that were added to the embryonic species determined their eventual fate, *e.g.*, the morphologies into which they would ultimately evolve. Extensive high-resolution transmission electron microscopy experiments revealed that the growth pathway—monomer addition, coalescence, or a combination of the two—was different for each of the morphologies, and was likely controlled by the interactions of each specific anionic adsorbate with the embryonic species. Similar phenomena were observed for related palladium and platinum nanoparticle systems. These studies provide important insights into how noble metal nanoparticles nucleate, the pathways by which they grow into several distinct morphologies, and the imperative role of the anonic ligand in controlling which route predominates in a particular system.

KEYWORDS: noble metal nanoparticles · nanoparticle synthesis · shape-controlled nanoparticles · nanoparticle formation · nanoparticle growth · transmission electron microscopy

The inherent physicochemical characteristics of colloidally synthesized nanoparticles, such as melting point,[1] catalytic activity,[2] electronic structure,[3] plasmon resonance,[4] magnetism,[5] and crystal structure,[6] often are distinct from those of their bulk analogues. In particular, noble metal nanoparticles have been widely studied because of their use in catalysis, photonics, electronics, sensing, and biomedicine.[7] For these and other applications, properties and performance can be tuned through prudent control of nanoparticle size, composition, and shape. For example, with a heterogeneous nanoparticle catalyst the size, composition, and shape help to define the ratio of surface-to-bulk atoms (and therefore the number and density of catalytically active sites), the electronic characteristics, and the surface-exposed crystal facets, respectively. All of these features therefore can impact the activity and

* Address correspondence to res20@psu.edu.

Received for review November 16, 2014 and accepted January 28, 2015.

Published online January 28, 2015
10.1021/nn506517e

selectivity for a given catalytic process. Accordingly, a thorough understanding of synthesis-structure relationships is imperative for rationally designing metal nanoparticles to achieve optimal performance in target applications.

Shape control is a powerful but challenging strategy for optimizing the properties of metal nanoparticles through the selective exposure of certain crystallographic facets. Common approaches include addition of shape-directing surface adsorbates or colloidal stabilizers,[8,9] prudent selection of reaction temperature or reducing agent,[10,11] controlled reagent addition rate,[12,13] and seed-mediated synthesis.[14,15] Shape-controlled noble metal nanoparticles are most commonly accessed through the selective adsorption of ligands, including halides and other small anions,[9] to certain crystallographic facets. However, access to distinct shapes with the same exposed crystal planes, such as octahedra and icosahedra bound by {111} facets, is difficult to rationalize within this framework and points to the complexity of the putative reaction pathways that underpin their formation. Indeed, colloidal routes routinely produce nanoparticles with many distinct shapes, but the pathways by which they form from molecular precursors, including similarities or differences that exist among different morphologies of the same material, often remain elusive and can be challenging to interrogate.[16]

The traditional LaMer model for nanoparticle formation is a two-step process consisting of nucleation and growth.[17−19] This model predicts that the monomer concentration will increase until it reaches a certain level of supersaturation, then homogeneous nucleation will occur in a "burst" in order to decrease the free energy of the system.[20] Nucleated particles below a critical size redissolve due to their high surface energy, whereas for stable particles larger than this size growth becomes energetically favorable.[21] Immediately thereafter, growth proceeds by monomer addition to the particles that nucleated during the "burst", and small nuclei are difficult to capture. For metals, the source of monomer is either the continued direct reduction of the precursors to zerovalent atoms or through Ostwald ripening, whereby smaller particles are sacrificially dissolved to contribute atoms to larger growing particles.[22,23] In contrast to this traditional model of nucleation and growth, recent computational[24,25] and experimental[26−30] studies suggest that clusters, which consist of only a few hundred atoms or less (roughly $\leq$2 nm), may serve as stable or metastable intermediates during the formation of colloidal nanoparticles. Experimental evidence supporting this alternate pathway has been limited, especially for metal nanoparticles, although stable clusters of noble metals have been synthesized using a variety of procedures, including the reduction of molecular precursors in the presence of poly(vinylpyrrolidone) (PVP).[31−35]

Nanoparticle growth can also proceed through the coalescence of smaller primary units, which is a distinct and complementary pathway to the classical monomer addition route. This was first reported by Penn and Banfield in TiO_2 nanostructures, which formed in solution by the oriented attachment of small nanoparticles.[36] Importantly, they also observed that twinning, dislocations, and other planar defects in the resultant crystal can form due to coalescent growth. Subsequently, coalescence has been identified as the primary mechanism of growth in many nanoscale metals and compounds,[28,37−41] with supporting experimental evidence coming from observations by *in situ* transmission electron microscopy (TEM)[27,42−44] and *in situ* small-angle X-ray scattering (SAXS).[45,46] The driving force for coalescence or oriented attachment between two primary particles is potentially system-dependent, but molecular dynamics simulations suggest that van der Waals forces, dipole−dipole interactions, adsorbate interactions, and surface−solvent effects all may play a role.[47,48] Growth by both coalescence and monomer addition has also been reported to occur concomitantly.[26,27,42] Therefore, identifying the experimental parameters that determine whether metal nanoparticle growth proceeds by monomer addition, coalescence, or a combination of the two is essential for better understanding the pathways by which nanoparticles form.

Here, we report a comprehensive study of the process by which colloidal noble metal nanoparticles having several distinct shapes nucleate and grow. We focus on the polyol synthesis of shape-controlled Rh nanoparticles. Rh is a highly studied catalytic metal nanoparticle system due to its strong resistance to heat and corrosion[49] combined with its ability to catalyze several important classes of chemical transformations, including oxidations, reductions, hydroformylations, and cross-couplings.[50−53] Three distinct morphologies were examined: single-crystalline cubes bound by {100} facets, multiply twinned icosahedra bound by {111} facets, and singly twinned triangular plates bound primarily by {110} facets. Analogous nanoparticle shapes of Pt and Pd were also studied for comparison and generalization. The polyol strategy that we used permitted fine control over the reaction variables.[30] Molecular precursors were heated in a polyol solvent to a threshold temperature that facilitated reduction and nucleation of small nanoparticle clusters, then to a higher temperature that initiated further growth and size focusing. This two-step reaction scheme resulted in the temporal separation of distinct growth phases that occur during the formation of the shape-controlled nanoparticles.[11] Through analysis of aliquots taken during the reactions,[5,10,29] we found that, for all morphologies, metal clusters with diameters of $\leq$2 nm first nucleated as a stable intermediate following precursor reduction and prior to the

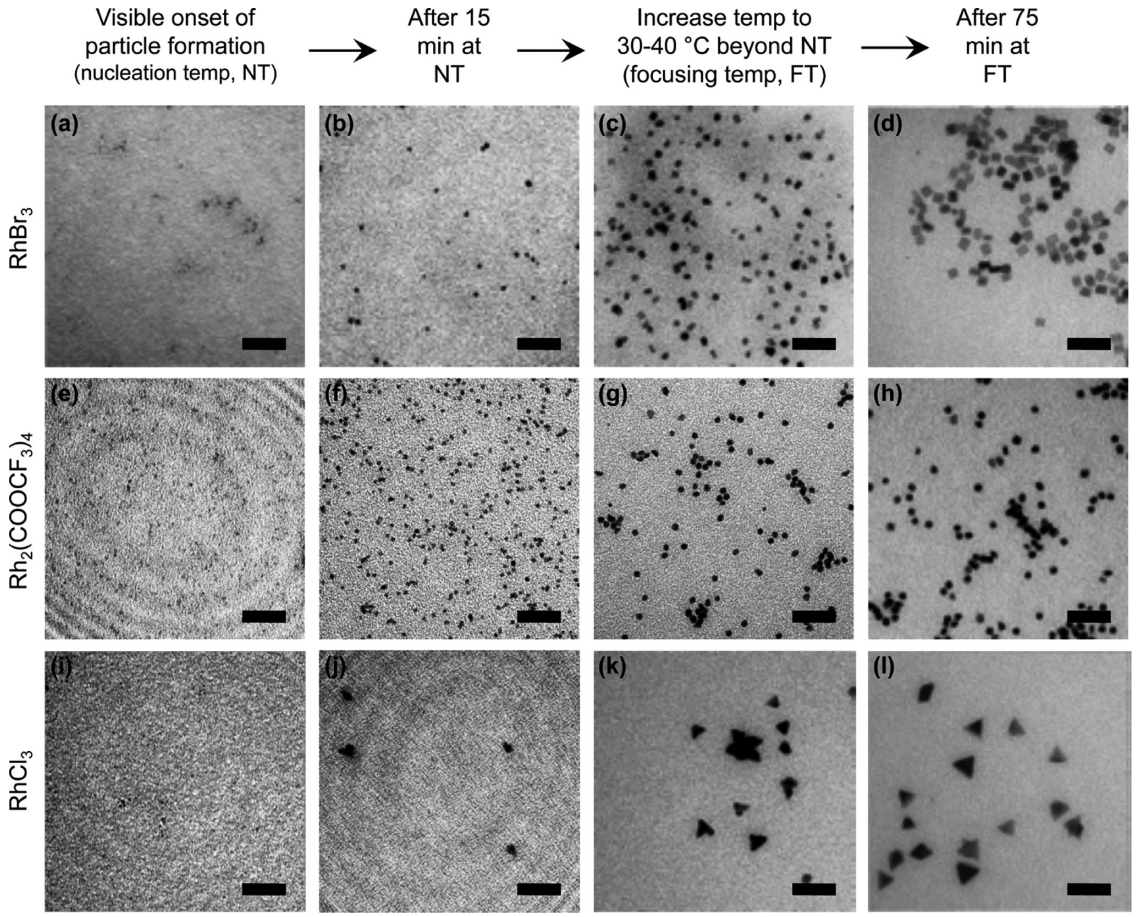

Figure 1. TEM images showing aliquots taken during the heat-up synthesis of Rh cubes from $RhBr_3$ in DEG (a–d), icosahedra from $Rh_2(COOCF_3)_4$ in EG (e–h), and triangular plates from $RhCl_3$ in TREG (i–l). Aliquots were collected at (a, e, and i) the temperature corresponding to the visible onset of particle nucleation, (b, f, and j) after 15 min maintaining that temperature, (c, g, and k) upon increasing the temperature 30–40 °C, and (d, h, and l) after 75 min of focusing at that temperature. Scale bars represent 20 nm.

initiation of widespread growth. Additionally, these nucleated clusters grew to form monodisperse metal nanoparticles of varying morphologies, depending on the identity of the ligand that was present when further growth was initiated. The metal cluster intermediates, which were colloidally stable in a stock solution, served as embryonic species, and the ligands that were added to them determined their eventual fate, *e.g.*, the morphologies into which they would ultimately grow. Extensive high-resolution TEM (HRTEM) revealed that the growth pathway—monomer addition, coalescence, or a combination of the two—was different for each of the different morphologies, and was likely controlled by the interactions of each specific anionic ligand with the metal surfaces.

RESULTS AND DISCUSSION

Formation of Rh Nanoparticle Cubes, Icosahedra, and Triangular Plates from Molecular Precursors. Colloidal Rh nanoparticles were synthesized by dissolving an appropriate Rh reagent and poly(vinylpyrrolidone) (PVP) stabilizer in a glycol-based polyol solvent and then heating this solution using a carefully controlled temperature program.[11] Previously identified optimal combinations of Rh reagents and polyol solvents are $RhBr_3$ in diethylene glycol (DEG) to produce cubes, $Rh_2(COOCF_3)_4$ in ethylene glycol (EG) to produce icosahedra, and $RhCl_3$ in triethylene glycol (TREG) to produce triangular plates.[11] Temporal separation of distinct growth phases to form monodisperse Rh nanoparticles with high morphological yield is achieved by first heating the Rh reagent, PVP stabilizer, and glycol solvent to an optimized nucleation temperature (NT) for 15 min, and then subsequently to a higher focusing temperature (FT) for 75 min.[18] For all reactions, aliquots were collected (1) upon reaching the NT; (2) after 15 min at the NT; (3) upon reaching the FT, which is typically 30–40 °C higher than the NT; and (4) after 75 min at the FT, at which time the reaction is complete. The aliquots were centrifuged, and both the solid product and the supernatant were analyzed by a suite of microscopic, spectroscopic, and diffraction tools.

Figure 1 shows TEM images of the precipitates collected from each of the aforementioned aliquots. Examination of the TEM images taken just as reduction has visibly commenced (Figure 1a,e,i), *e.g.*, when the

reaction solutions begin to darken and turn slightly brown, revealed polydisperse 1−2 nm clusters, corresponding to between 100 and several hundred atoms stabilized by PVP.[54] These clusters are roughly spherical, to minimize surface energy,[55] despite the disparate morphologies of the eventual products; smaller clusters not discernible by TEM likely exist concomitantly. HRTEM analysis of the clusters collected during the initial stages of the reactions revealed no observable lattice fringes and produced no powder X-ray diffraction (XRD) reflections, indicating a lack of long-range atomic order.[12] After maintaining the reaction at the NT for 15 min (Figure 1b,f,j), a bimodal distribution of the Rh clusters and larger seed particles, with diameters of approximately 3−4 nm, was present. (We consider a "seed" to be a particle for which growth has recently commenced, affording it a clearly discernible size, morphology, and often crystallinity by TEM, as opposed to ≤2 nm clusters, which have nucleated in solution but for which growth has not yet initiated.) However, upon heating the reaction solution an additional 30−40 °C to the FT, particle growth had initiated in earnest (Figure 1c,g,k). For all three systems, the mean size of the particles at the FT was more than twice that of the previous aliquot, and the morphologies could be clearly differentiated into discernible truncated cubes (Figure 1c), pseudospherical polyhedra (Figure 1g), and anisotropic 3-fold branched particles (Figure 1k). Concurrently, the cluster population in the images appeared to decrease significantly compared to the second aliquot, although some were still present. Finally, the particles were held at the FT for 75 min before being quenched with cold water. The mean particle sizes had increased slightly, and the products, which were well-formed cubes, icosahedra, and triangular plates with uniform faces, corners, and edges, were now largely monodisperse colloidal nanoparticles (Figure 1d,h,l). Rh clusters were no longer visible in the product, implying that all of the atoms that comprised them had been incorporated into the product nanoparticles.

High-angle annular dark field scanning TEM (HAADF-STEM), which more effectively distinguishes the heavier-atom Rh clusters and atoms from the lighter-atom support because of its exceptional Z-contrast imaging capabilities,[28,33,56−58] was also used to analyze each aliquot with respect to the presence or absence of Rh clusters. Figure 2 and Supporting Information Figures S1 and S2 confirm the formation of Rh clusters with a distribution of sizes ranging from 1−2 nm at the onset of reduction. HAADF-STEM analysis also confirmed that a mixture of clusters and larger seed particles are visible after 15 min at the NT and that larger nanoparticles were now the primary species present, along with a significantly smaller population of clusters, upon reaching the FT. Finally, HAADF-STEM confirmed that no clusters were visible,

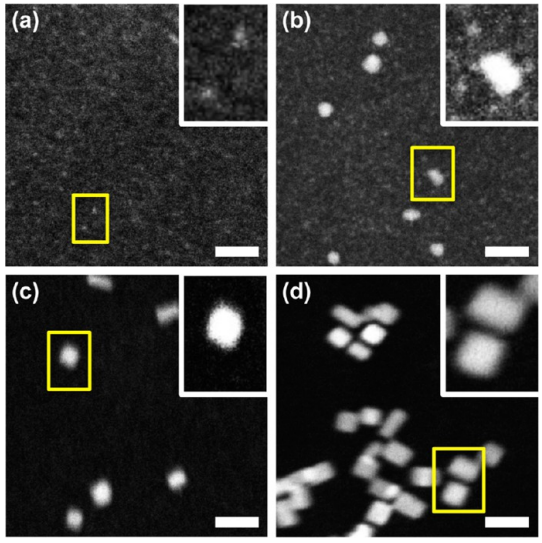

Figure 2. HAADF-STEM images showing aliquots taken during the formation of Rh cubes by heat-up synthesis using $RhBr_3$ in DEG. Insets are enlarged from the regions outlined in yellow. These images correspond to the samples in Figure 1a−d. Aliquots were collected (a) upon visible onset of nucleation at 110 °C, (b) after 15 min at 110 °C, (c) upon reaching the focusing temperature of 140 °C, and (d) after 75 min at 140 °C. Scale bars represent 10 nm.

with only well-formed nanoparticles present, after 75 min at the FT. That particle growth is arrested only when the population of clusters diminishes suggests that these clusters could be a primary source of monomer during the growth of the metal nanoparticles, and therefore an intermediate species between the molecular precursor and the resulting metal nanoparticle product.

UV−visible (UV−vis) absorption spectroscopy was used to analyze both the precipitates, which were isolated and resuspended as colloidally stable particles in ethanol, and the supernatants of each aliquot, as well as several control samples for comparison (Figure 3 and Supporting Information Figures S3−S6). Figure 3 shows the UV−vis absorption spectra corresponding to the formation of Rh icosahedra. For all aliquots, the spectra for both the precipitates and the supernatants were dominated by an absorbance peak at 226 nm, corresponding to the PVP (Supporting Information Figure S4) that is both adsorbed to the surface of the particles and free in the supernatant solution. Absorbance due to the surface plasmon resonance (SPR) of Rh nanoparticles lies in the UV region[11,12,54] and was discernible for the icosahedra from approximately 240 to 320 nm. The UV−vis spectrum of the precipitate indicated that as the particles grew larger in size, the intensity of the SPR absorbance also increased relative to that of PVP. This was also true for the other morphologies (Supporting Information Figures S5a and S6a), although the SPR absorbance for Rh nanoparticles was shape-dependent, falling at ∼250−350 nm for the cubes and ∼300−400 nm

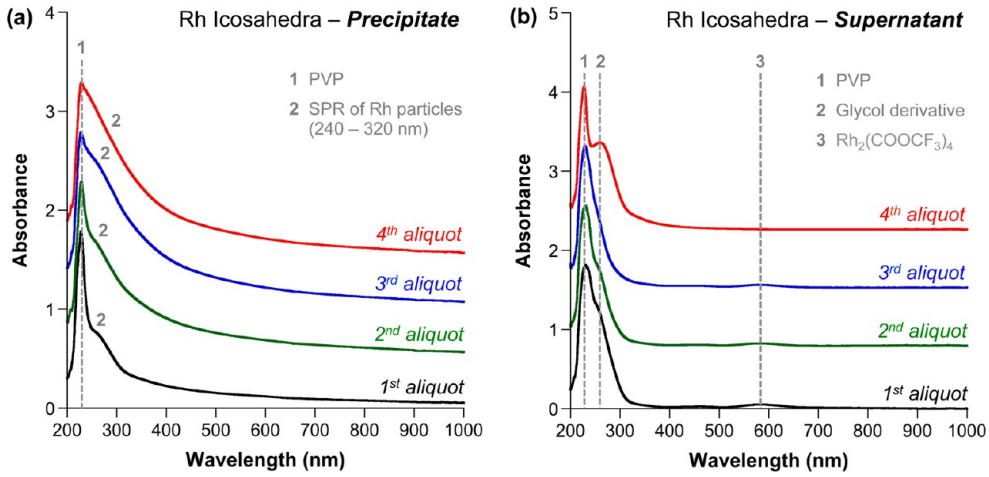

Figure 3. Normalized UV−vis absorption spectra in EG collected from the separated (a) precipitates and (b) supernatants of aliquots taken during the formation of Rh icosahedra.

for the triangular plates. We attribute the rising baseline absorbance in the third and fourth aliquots to increased light scattering by particles after growth initiates compared to the clusters that form at the onset of precursor reduction.[59]

UV−vis spectra of the supernatants corresponding to the first three aliquots taken during the formation of the Rh icosahedra (Figure 3b) revealed an absorbance centered at 580 nm, which indicated that $Rh_2(COOCF_3)_4$ was present (Supporting Information Figure S3). Consistent with this, these supernatants appeared a teal blue color that matched well with that of the $Rh_2(COOCF_3)_4$ precursor, while that of the final product was colorless (Supporting Information Figure S7). This indicated that unreduced precursor was still present in solution when the FT was reached, and this will contribute monomer to the growth of crystalline nanoparticles, either directly or through Rh cluster intermediates. Evidence of unreduced precursor was also observed in the first three aliquots of the Rh cube ($RhBr_3$) and Rh triangular plate ($RhCl_3$) systems (Supporting Information Figures S5b and S6b). In all of these cases, the Rh precursors were not completely reduced to Rh^0 until the final aliquot. The UV−vis spectra of all aliquot supernatants had an absorbance at 226 nm, which is attributed to excess PVP. Notably, the UV−vis spectrum in Figure 3b obtained from the supernatant of the final aliquot, which consisted of fully formed Rh icosahedra, was dominated by a peak that developed around 257 nm. This absorbance is attributed to an organic species that formed as a byproduct of ethylene glycol (EG) oxidation. Previous reports have indicated that EG is oxidized to either acetaldehyde or glycoaldehyde,[60] which are likely further oxidized to other derivatives such as diacetyl, glycolic acid, and oxalic acid.[61,62] UV−vis spectra of plausible organic species (Supporting Information Figure S4) indicated that oxalic acid dissolved in EG had an absorbance spectrum similar to the final supernatant in Figure 3. The presence of oxalic acid in the supernatant is feasible due to its stability and low volatility, whereas many of the other possible derivatives are either reactive or would boil off at the reaction temperature.[63] The final supernatants collected from the cube and triangular plate syntheses (which have different reducing solvents with greater molecular complexity) showed similar absorbance values that were likely due to one or more glycol-derived species, including glyoxal, which has a similar absorbance signature.

The collective observations from TEM, HAADF-STEM, and UV−vis analysis of aliquots are consistent with a general pathway by which the Rh nanoparticles form using the polyol method. The onset of reduction and the formation of Rh clusters occurs at the NT, which is defined by the collective redox potentials of the precursor and the solvent. Reduction continues and some seed particles form upon holding at the NT for 15 min. Heating the solution an additional 15−20 °C initiates nanoparticle growth, and maintaining the reaction at a FT 30−40 °C above the NT allows for complete reduction of the Rh precursor. By this point, the clusters are visually absent and their atoms have been presumably incorporated into the final monodisperse nanoparticle product. However, some key questions remain. First, the process by which atoms and clusters present in solution add to growing particles is not known. While there have been previous reports of 1−2 nm particles acting as an intermediate to nanoparticle formation, in some cases growth occurs by monomer addition (Ostwald ripening) and in other cases by coalescence.[37,42] Second, although the presence of Cl^-, Br^-, or $COOCF_3^-$ clearly influences the morphological outcome of the reaction, the specific pathways by which the different morphologies emerge is not apparent. Third, the nature of the clusters that form initially and their role in shape-selective synthesis is uncertain. Importantly, distinct morphological

characteristics generally were not evident until the later stages of each reaction, and the Rh clusters that initially formed appeared indistinguishable, despite their eventual discrimination. Accordingly, the studies below help to provide a more comprehensive understanding of the pathways by which the Rh clusters evolve into icosahedra, cubes, and triangular plates based on the ligands that are present.

High-Yield Synthesis and Characterization of Stable Rh Clusters. To more thoroughly study the formation and morphological evolution of the Rh clusters that appeared in the early stages of the reaction, we modified the conditions to selectively produce clusters without initiating their growth into larger seed particles. TEM (Figure 4a) and HAADF-STEM (Supporting Information Figure S8a) images of the product obtained when heating $RhCl_3$/PVP in TREG to 100 °C for 75 min, which is a lower temperature and longer time than used previously, confirmed the high-yield synthesis of metal clusters having diameters of 2 nm or less. These Rh clusters were colloidally stable for weeks when dispersed in polar media and kept at room temperature.

The UV−vis spectrum of the Rh clusters in TREG was dominated by PVP at 226 nm, with additional low absorbance extending up to 540 nm that is likely due to SPR[31,64] and scattering[59] of the clusters (Figure 4a). This is in contrast to the spectrum of $RhCl_3$ in TREG, which absorbs most strongly at 247 nm and absorbs up to 600 nm. Additionally, the solutions were visually distinct (Supporting Information Figure S8b). These observations suggest that after 75 min at 100 °C, the vast majority of $RhCl_3$ had been reduced to Rh clusters. To quantify this, the colloidal Rh clusters were separated from the unreduced molecular $RhCl_3$ precursor by centrifugation, and inductively coupled plasma atomic emission spectroscopy (ICP−AES) was used to determine the Rh content of both the precipitate and the supernatant. The concentration of Rh in the precipitate was more than five times greater than that of the supernatant, and the yield of $RhCl_3$ reduction was calculated to be 84.5%. This indicated that nearly all of the initial Rh from the $RhCl_3$ precursor incorporated into the clusters. Consistent with this, UV−vis spectra indicated that the supernatant was mostly colorless, with only a very low absorbance centered at 237 nm, which we attribute to a mixture of PVP, glycol derivative, and a small amount of unreacted $RhCl_3$ (Supporting Information Figure S9). Importantly, no absorption peak attributable to $RhCl_3$ was observed in the UV−vis spectrum of the precipitate.

X-ray photoelectron spectroscopy (XPS) revealed that the Rh clusters had an oxidation state intermediate between that of the $RhCl_3$ precursor and the Rh nanoparticle product (Supporting Information Figure S10), consistent with the small particle size and the high percentage of undercoordinated Rh^0 atoms in the 1−2 nm clusters. XPS also indicated that

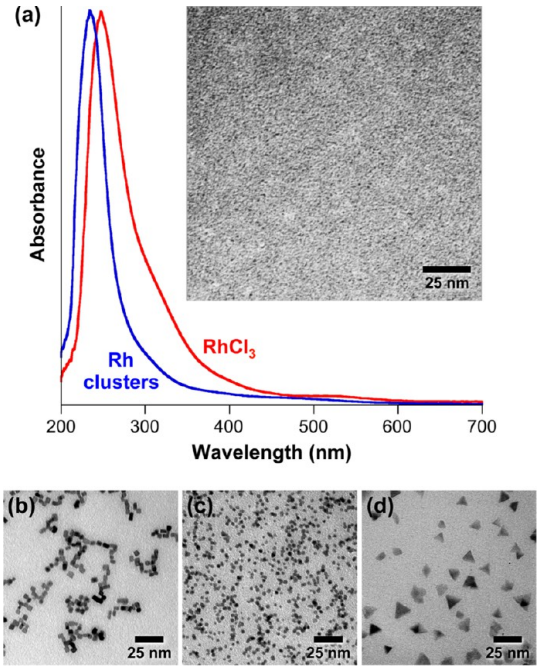

Figure 4. (a) Normalized UV−vis absorption spectra in TREG of $RhCl_3$ and Rh clusters, confirming the absence of $RhCl_3$ in Rh clusters due to reduction. Inset: TEM image of Rh clusters synthesized from $RhCl_3$ in TREG. (b−d) TEM images of (b) Rh cubes, (c) Rh icosahedra, and (d) Rh triangular plates synthesized from the same lot of Rh/PVP clusters derived from $RhCl_3$, but using different anionic additives. NaBr was added in the synthesis of Rh cubes in (b), $NaCOOCF_3$ was added in the synthesis of Rh icosahedra in (c), and no additive was added in the synthesis of triangular nanoplates in (d), as they already contain Cl^-.

significant Cl^- was present, likely adsorbed to the Rh surface atoms along with PVP. Small-angle X-ray scattering (SAXS) indicated that most of the Rh particles had a diameter in the range of 2.5−4.5 nm, with an average of 3.6 ± 1 nm, confirming that a distribution of sizes was present (Supporting Information Figure S11). The SAXS diameter includes the PVP layer surrounding the Rh clusters, so is therefore larger than the diameter observed by TEM, as expected. SAXS also confirmed that a small population of seed particles or agglomerates 8−14 nm in diameter was present, as observed also by HAADF-STEM (Supporting Information Figure S8a).

Importantly, we found that the high-yield stock solution of Rh clusters described in the preceding paragraphs could be used to generate all three morphologies of Rh nanoparticles[65] (cubes, icosahedra, and triangular plates) by varying the ligand environment through salt additives and without the need for processing to achieve morphological uniformity (Figure 4b−d).[14] Continuing to heat the $RhCl_3$-derived Rh clusters (which have Cl^- present in solution) resulted in the formation of Rh triangular plates. However, when NaBr (a source of Br^-) was added prior to heating the Rh cluster solution to the FT, Rh cubes formed. Likewise, when $NaCOOCF_3$ (a source of $COOCF_3^-$) was added, Rh icosahedra formed.

The ability to use a stock solution of stable Rh clusters as the precursor for forming each of these morphologies allowed us to decouple the distinct stages of formation and made apparent that the later stage of growth (after the stable Rh clusters form) was the driving force behind the shape-controlled synthesis of Rh nanoparticles. Further, by using a similar reaction temperature and solvent/stabilizer system, we can posit that the primary synthetic lever for morphological control is the anionic ligands that are available to coordinate to the nanoparticle, but their effect as shape-directing agents is only realized once the final growth stage of the reaction initiates. With these insights, we sought to investigate how equivalent clusters can form three distinct nanoparticle morphologies, why the ligand environment drives these divergent crystallization pathways, and at what point during the nanoparticle formation process this deviation occurs.

Analysis of Rh Nanoparticle Formation by the Directed Crystallization of Rh Cluster Precursors. Temporal evaluation of the Rh nanoparticle formation pathway was provided by using TEM, HAADF-STEM, UV−vis, and especially HRTEM[66] to monitor the process by which the stock solution of Rh cluster precursors transformed into Rh cubes, icosahedra, and triangular plates in the presence of Br^-, $COOCF_3^-$, and Cl^-, respectively. The same cluster precursor and solvent were utilized for each morphology to allow direct comparison of their formation routes. For each system, nine aliquots were analyzed. The aliquots were acquired at temperatures 15 and 7 °C lower than the FT, upon reaching the FT, and after holding at that FT for 2.5, 5, 10, 20, 45, and 75 min. Supporting Information Figures S12−S17 show TEM and HAADF-STEM images of each aliquot taken during the formation of Rh cubes (Supporting Information Figures S12 and S13), icosahedra (Supporting Information Figures S14 and S15), and triangular plates (Supporting Information Figures S16 and S17), respectively, and the images presented are representative of what is observed globally during these crystallization processes. These TEM and HAADF-STEM images clearly show the evolution from Rh clusters to larger seed particles, and finally to the morphologically distinct final products. This confirmed that the nanocrystals form *via* the same general pathway when starting with the presynthesized stock solution of Rh clusters as they do *in situ* during the traditional heat-up synthesis directly from the molecular Rh precursors. UV−vis absorbance spectra of the purified aliquots confirmed the development of the broad absorbances due to the SPR of the three Rh nanoparticle morphologies (Supporting Information Figures S18−S20).

Starting with the Rh cluster stock solution, Rh cubes with a 90% morphological yield and a mean diameter (measured across the hypotenuse) of 7.1 ± 0.9 nm formed upon adding NaBr and heating to a FT of 140 °C for 75 min. Similarly, Rh icosahedra with a 92% morphological yield and a mean diameter of 4.4 ± 0.5 nm formed upon adding $NaCOOCF_3$ and heating to a FT of 125 °C for 75 min. Finally, Rh triangular plates formed with a morphological yield of 79% and a mean diameter (measured from tip to opposite base) of 10.2 ± 1.8 nm upon heating to a FT of 135 °C for 75 min when no additional anionic additives were added; Cl^- was already present since $RhCl_3$ was the Rh precursor used to make the Rh cluster stock solution. The shape selectivities and size distributions for each of these Rh nanoparticle morphologies were comparable to those in previous reports.[11,67]

HRTEM images of Rh nanoparticles observed in aliquots taken 0 min (FT_0), 2.5 min ($FT_{2.5}$), 5 min (FT_5), and 10 min (FT_{10}) after reaching the FT in the NaBr/Rh system, which produced cubes, are shown in Figure 5 and Supporting Information Figure S21. Perhaps due to the high melting point of Rh relative to other noble metals, these Rh nanoparticle intermediates were stable during HRTEM imaging and no restructuring was observed at short time scales. At FT_0, we observed 3−5 nm single-crystalline seed particles with lattice spacings and a fast Fourier transform (FFT) corresponding to Rh{111} (Figure 5a), in contrast to the {100} facets that will eventually develop. The quasi-spherical shape of the seed particles suggested that they were cuboctahedra bound by a mixture of Rh{111} and Rh{100} planes, as has been reported for other fcc metal nanoparticles,[7] and is consistent with the Wulff construction.[68] HRTEM imaging of subsequent aliquots showed that as the particles continued to grow larger, the {100} facets became more dominant (Figure 5c) as they were stabilized by Br^- adsorbates[11] and the higher-energy {111} planes were preferentially grown in.[7] Note that cubes are known to form due to Br^- selectively coordinating to and stabilizing the {100} planes of Rh.[67] A HRTEM image and corresponding FFT of a fully formed Rh nanocube viewed along the [001] zone axis is shown in Figure 5e. The particle was single-crystalline with lattice fringes of 1.9 Å that corresponded to the (200)/(020) planes of Rh, confirming that the cube was bound by six {100} facets. A mixture of cuboctahedra and truncated cubes was observed during the growth of the final Rh nanocrystal cubes. Importantly, no twin boundaries were present and coalescence events were not observed, as the growth appeared to be in a purely epitaxial manner with overgrowth of the cuboctahedral seeds to form cubes. There was not enough dissolved Rh precursor from the residual $RhCl_3$ in the Rh cluster stock solution (verified by ICP and UV−vis, as described in the previous section) to account for the evolution of all of the Rh clusters into nanocrystalline cubes *via* a direct monomer addition pathway. This suggested, therefore, that Ostwald ripening was the dominant growth process in the Rh nanocube system, with the Rh clusters dissolving to act as the primary source of Rh monomer.

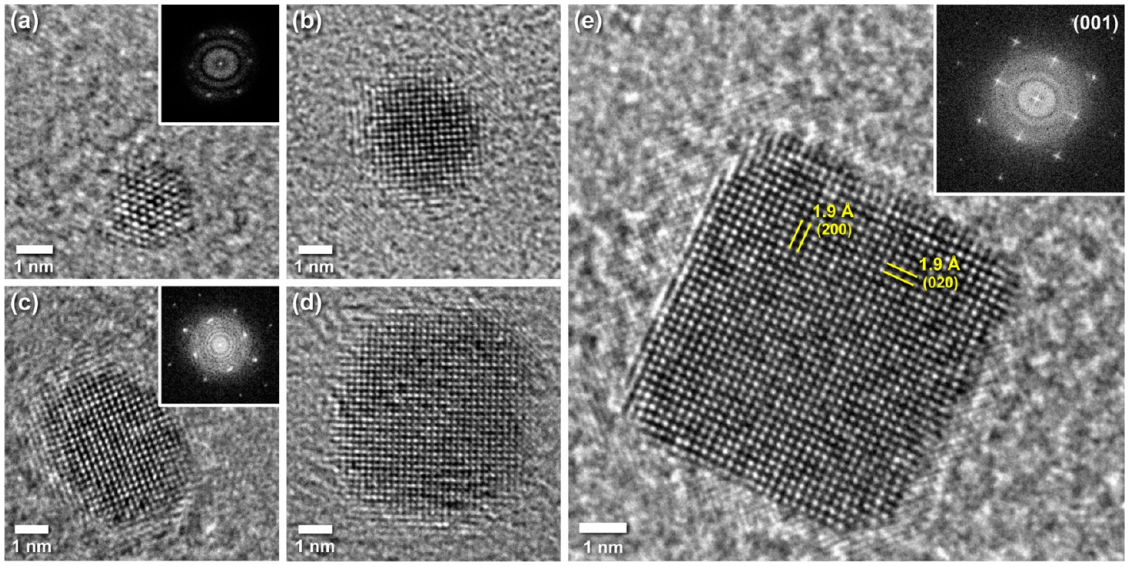

Figure 5. HRTEM images of particles observed during the formation of Rh cubes from Rh/PVP cluster precursors in the presence of NaBr. Aliquots were taken (a) upon reaching the FT of 140 °C, (b) after 2.5 min at the FT, (c) after 5 min at the FT, and (d) after 10 min at the FT. A representative nanocube product is shown in (e). Insets show the FFT of each particle. The data indicate that the growth of Rh cubes proceeds epitaxially from cuboctahedral seeds with a mixture of {111} and {100} facets, ultimately producing exclusively {100} facets.

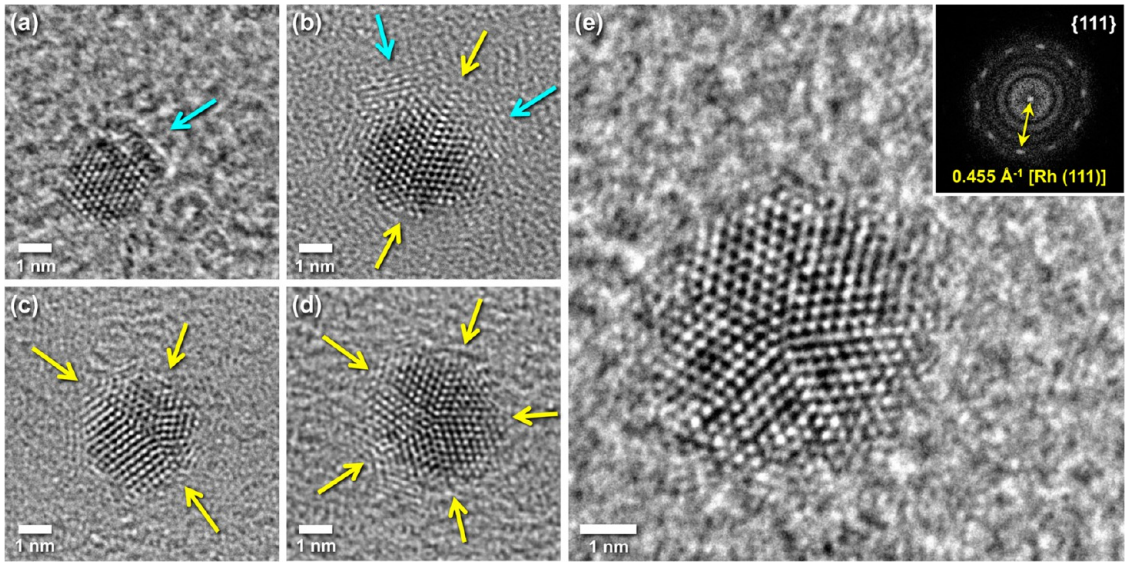

Figure 6. HRTEM images of particles observed during the formation of Rh icosahedra from Rh/PVP cluster precursors in the presence of $NaCOOCF_3$. Aliquots were taken (a) upon reaching the FT of 125 °C, (b) after 2.5 min at the FT, (c) after 5 min at the FT, and (d) after 10 min at the FT. A representative icosahedron product is shown in (e) with its FFT as the inset. Yellow arrows mark twin boundaries and cyan arrows indicate coalescence events. The data suggest that the growth of Rh icosahedra proceeds through coalescence of single-crystalline 3−4 nm particles with clusters to form multiply twinned, and eventually icosahedral, seeds. These twinned seeds then grow epitaxially to form icosahedra with exposed {111} facets.

HRTEM images corresponding to the formation of Rh icosahedra in the presence of added $NaCOOCF_3$ to the Rh cluster stock solution are shown in Figure 6 and Supporting Information Figure S22. Icosahedra consist of 20 tetrahedra joined by their {111} facets along twin boundaries.[69] This implies that the $COOCF_3^-$ anion leads to the selective formation of Rh{111} and also facilitates multiple twinning events. Interestingly, rather than being twinned, the 3−4 nm particles that formed initially were single-crystalline, likely of a cuboctahedral or truncated octahedral morphology, with Rh{111} facets primarily exposed (Supporting Information Figure S22b). However, by the point that the FT was reached, evidence for coalescence events was observed between the single-crystalline particles and smaller cluster particles (Figure 6 and Supporting Information Figure S22, cyan arrows). At $FT_{2.5}$, singly twinned particles with grain boundaries (Figure 6, yellow arrows) were readily seen, with continued coalescence events between these particles and smaller

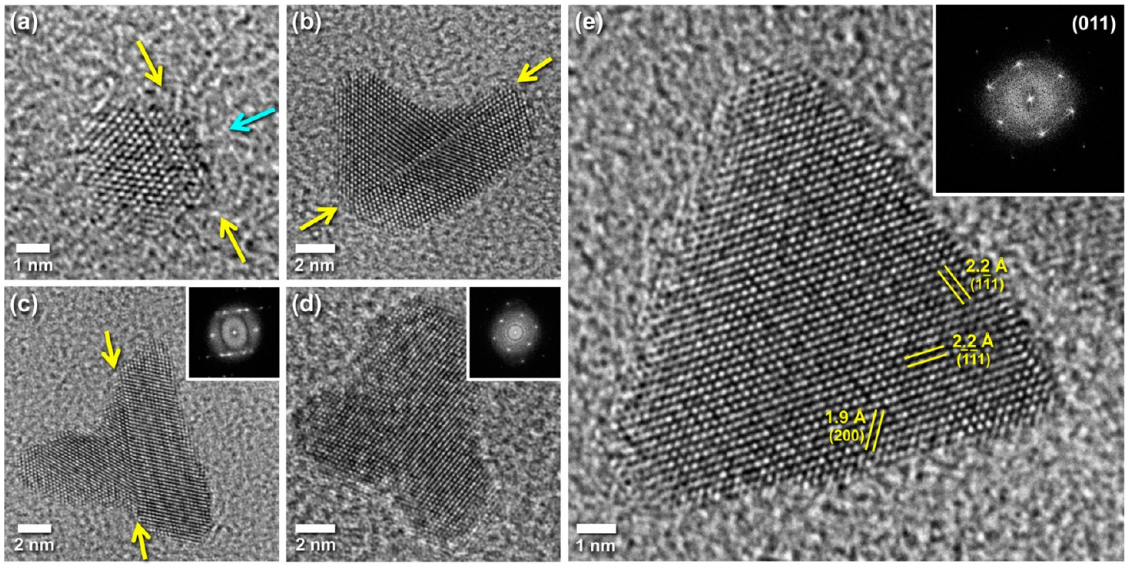

Figure 7. HRTEM images of particles observed during the formation of Rh triangular plates from Rh/PVP cluster precursors with no additives. Aliquots were taken (a) upon reaching the FT of 135 °C, (b) after 2.5 min at the FT, (c) after 5 min at the FT, and (d) after 10 min at the FT. A representative triangular nanoplate product is shown in (e). Insets show the FFT of each particle. Yellow arrows mark twin boundaries and the cyan arrow indicates a coalescence event. The data suggest that the growth of Rh triangular nanoplates proceeds through coalescence of single-crystalline 3−5 nm particles with clusters to form singly twinned seeds, then anisotropic growth to 3-fold branched particles, followed by monomer addition between the branches and atomic rearrangement to form triangular plates with single-crystalline {110} faces.

clusters occurring. By FT_5, multiply twinned particles were prevalent. Collectively, these observations imply that coalescence is responsible for the formation of twin defects in these growing nanoparticles. Although previous reports have indicated that single-crystalline particles can grow by coalescence with retention of the underlying atomic structure,[39] in this case the observations suggest that misorientation between the two coalescing particles is the primary cause of twin boundary formation.[36] Presumably to minimize the overall surface energy of the multiply twinned crystals, the growing nanoparticles undergo an internal rearrangement such that by FT_{10} they have formed an icosahedral seed.[10,44] Since the majority of the particles already assumed an icosahedral morphology by FT_{10}, further growth (responsible for the mean particle size increasing from 3.9 to 4.4 nm) is hypothesized to have proceeded through epitaxial overgrowth of the seed *via* dissolution of the remaining clusters by Ostwald ripening before arriving at the final icosahedral product. Figure 6e shows an HRTEM image of a fully formed Rh nanoicosahedron viewed close to a 5-fold axis of symmetry. These polycrystalline particles were bound by Rh{111} facets with lattice fringes of 2.20 Å, as indicated by the corresponding FFT.

HRTEM images corresponding to aliquots taken during the formation of Rh triangular plates are shown in Figure 7 and Supporting Information Figure S23. Much like for the cubes and icosahedra, the 3−5 nm particles that formed initially are single-crystalline. However, coalescence (Figure 7a, cyan arrow) led to the formation of singly twinned seed particles (Figure 7, yellow arrows), most of which had branched arms by $FT_{2.5}$. It is important to note that, as with the Rh icosahedra, coalescence appeared to be responsible for the development of twin defects, and metal nanoparticles with triangular shapes have previously been observed to contain a single twin defect.[70] Once twinned seeds had formed, growth occurred anisotropically, primarily on the three branches that evolved from each seed. Coalescence was not observed to occur along these branches, making monomer addition the likely mechanism of branch formation. At FT_5 there was a mixture of branched particles in various stages of formation and Rh clusters, which was presumably the source of monomer (*via* Ostwald ripening) for the growing particles. A majority of these particles still were singly twinned with multiple facets that could be indexed to Rh{110} planes (Figure 7c, FFT inset). However, grain boundary migration and internal rearrangement[40] eventually led (putatively) to the formation of a single-crystalline face on the planar particles, with the (110) plane of Rh selectively exposed (Figure 7d, FFT inset). Concurrently, particle growth occurred primarily between the arms of the 3-fold branched particles, with addition in these locations likely resulting in the greatest decrease in surface energy and in the voids being filled to form triangular nanoplates.

The formation route described above, with a singly twinned seed and a branched intermediate, is distinct from mechanisms that were suggested previously.[71,72] HRTEM imaging of a Rh triangular nanoplate (Figure 7e) oriented along the [011] axis revealed lattice fringes in

two directions of 2.2 Å, which corresponded to (111) planes, and in a third direction of 1.9 Å, which corresponded to Rh(200). The FFT of the particle image produced a pattern that was indexed to a single-crystalline (110) plane of Rh. The broad facet of exposed Rh(110) found on these particles is particularly interesting because previous reports[70,71] of fcc metal triangular plates, including our own,[11] indicated a (111) arrangement of atoms on their face, and also because there are few routes to fcc metal nanoparticles bound primarily by {110} planes.[73] It is difficult to determine unambiguously the crystallographic orientation of the facets that bind the edges of the triangular plates, but assuming they are orthogonal to the broad (110) face, two (111) and one (100) planes would be most likely to comprise the other facets of these nanoparticles.

Insights into the Shape-Controlled Polyol Synthesis of Rh Nanoparticles. Collectively, the results of these studies provide important insights into the polyol synthesis of shape-controlled Rh nanoparticles. In contrast to the LaMer model, which involves a burst of nucleation from a supersaturated monomer solution with subsequent solvated atoms adding directly onto these growing nuclei, we have observed that metal clusters form gradually throughout the nanoparticle formation process. Further, there appear to be multiple pathways by which the final shape-controlled particles grow: dissolution of small clusters for monomer addition (Ostwald ripening) or coalescence of clusters with the growing particle. However, most importantly, both observed growth mechanisms rely on the initial formation of clusters as intermediate species between the molecular precursors and the crystalline colloidal products, and our observations suggest that these initially formed clusters span a distribution of sizes and shapes and therefore are not "magic number" clusters.[31,32,34]

Although the Rh clusters all assume pseudospherical geometries following nucleation, the growth process can lead to several distinct nanoparticle morphologies in high yield. Our observations suggest that the resultant shape is largely dictated by the nature of the seed particles that form after the clusters, especially with regards to their crystallinity: single-crystalline, singly twinned, or multiply twinned. The formation of twins in the seed is particularly important for the evolution of anisotropic products or structural intermediates.[72] In turn, the crystallinity of the seed appears to depend primarily upon its formation pathway, specifically whether it develops by monomer addition, coalescence, or a combination of both processes. Our observations point to the ligand environment present during particle formation as the primary determinant of the growth process. In the case of metal nanoparticles, the ligands are anionic species. Specifically, 1−2 nm Rh clusters will form 3−4 nm seed particles with distinct crystallinities in different ligand environments, including single-crystalline seeds in the presence of Br^-, multiply twinned seeds in the presence of $COOCF_3^-$, and singly twinned seeds in the presence of Cl^-.

We hypothesize that these disparate growth processes can be rationalized based on the relative strengths by which these different ligands adsorb to the metal surfaces.[39] Br^- is known to strongly adsorb to the surface of Rh and other noble metals,[67] and this was confirmed by XPS (Supporting Information Figure S24). In contrast, $COOCF_3^-$ adsorbs only weakly. The varying adsorption strengths were observed during competition experiments by adding multiple anions during the growth phase. A 1:1 ratio of Br^-:Cl^- during Rh nanoparticle formation resulted in mostly cubes, due to the stronger adsorption energy of Br^- relative to Cl^-. However, a 1:1 ratio of $COOCF_3^-$:Cl^- resulted entirely in triangular plates, due to the weaker adsorption of $COOCF_3^-$ to the surface of Rh relative to that of Cl^-. Accordingly, we found that in order to form icosahedra in high yield from Rh clusters derived from $RhCl_3$, a 12-fold excess of $COOCF_3^-$ compared to the incipient Cl^- was needed. This suggests that the relative adsorption strengths of these anionic ligands to the Rh nanoparticle surface is $Br^- > Cl^- \gg COOCF_3^-$. Comparing this trend in adsorption energies with the pathways by which the various shapes emerge (monomer addition yielding cubes with Br^-, coalescence yielding icosahedra with $COOCF_3^-$, and a combination of coalescence and monomer addition yielding triangular plates with Cl^-) suggests a correlation between the ligand binding strengths and the nanoparticle formation pathway. When a surface is strongly "capped" by a ligand, coalescence is disfavored, likely due to the electrostatic repulsion of the adsorbate species or a lack of van der Waals interactions between particle surfaces.[13,40] However, weaker adsorbates have greater mobility on the surface, allowing for growing particles and clusters to overcome repulsion and come in contact with each other to coalesce. It should be noted, however, that for all morphologies monomer addition was observed following the ligand-determined formation of the seed particle, in accordance with *in situ* TEM observations that coalescence events are more common for smaller particles.[42] The growth process ceased when clusters were no longer present, as there was no longer a source of monomer.

Application to Other Noble Metal Nanoparticle Systems. Although the preceding studies and analyses focused on Rh nanoparticles, we anticipated that these principles may be applicable to other shape-controlled metal nanoparticle systems synthesized using the polyol process. Accordingly, we synthesized Pt cubes, Pt spheres, and Pd spheres using an analogous heat-up process in EG, taking and analyzing aliquots during their formation (Supporting Information Figures S25−S27). Analogous to the Rh system, 1−2 nm metal clusters formed initially as reaction intermediates between the

molecular precursor and the crystalline nanoparticle products. The 1−2 nm clusters were no longer observed in the final products, suggesting that their atoms were all incorporated into the nanoparticles through either coalescence or Ostwald ripening. Additionally, in the presence of Br^- ligands, which are known to adsorb strongly to the surface of Pt,[13,67] single-crystalline cubes were formed, likely through a monomer-addition growth pathway. Conversely, in the presence of more weakly adsorbing Cl^- ligands, multiply twinned particles formed, likely due to coalescence events occurring during the growth process between the more weakly capped particles. Collectively, these results suggest that, for systems in similar thermal and solvent regimes, the ligand is the primary determinant of the growth pathway—monomer addition, coalescence, or a combination of both—and ultimately the resulting morphology of colloidal metal nanoparticles.

CONCLUSIONS

In this contribution, we elucidated several important insights into the formation of metal nanoparticles using the polyol process, which is a common route to colloidal noble metal nanoparticles for plasmonic and catalytic applications. We showed that, for Rh nanoparticles, 1−2 nm PVP-stabilized colloidal cluster intermediates nucleated from solution initially. These Rh clusters were then synthesized in high yield and isolated without initiating further growth, thereby temporally separating the distinct growth stages throughout the reaction. Further, we showed that these metal clusters acted as stable reaction intermediates, which could be collected and subsequently used to form a variety of shape-controlled Rh nanoparticles following the thermal initiation of growth. Importantly, we related the ligand environment present during colloidal metal nanoparticle growth to both the resultant morphology *and* the pathway responsible for the formation of that morphology. On the basis of these observations, we proposed that the anionic ligands influenced not only the crystallographic planes that are thermodynamically favored in the product, but also the type of crystallinity that is favored. HRTEM analysis suggested that twinned nanoparticles are likely to result when particle growth occurs in the presence of a weakly bound ligand, due to a proliferation of coalescence events that occur during formation. In contrast, a strongly bound ligand appeared to promote epitaxial growth by Ostwald ripening, resulting in single-crystalline products. For Rh nanoparticles, strongly bound Br^- favored the formation of single-crystalline cubes by monomer addition, weakly bound $COOCF_3^-$ favored the formation of multiply twined icosahedra by coalescence, and moderately bound Cl^- favored the formation of singly twined triangular plates by a combination of coalescence and monomer addition. In all cases, growth largely halted once the supply of metal cluster precursors present in solution was exhausted, suggesting that these were indeed the primary source of Rh atoms that added to the growing nanoparticles. Finally, we showed that the insights provided by the Rh nanoparticle systems were likely general to the synthesis of other noble metal nanoparticles by polyol routes, as demonstrated preliminarily for Pt and Pd.

MATERIALS AND METHODS

Materials. Rhodium(III) chloride hydrate ($RhCl_3 \cdot xH_2O$, Rh 38.5−45.5%), rhodium(III) bromide hydrate ($RhBr_3 \cdot xH_2O$), dihydrogen hexachloroplatinate (IV) hydrate ($H_2PtCl_6 \cdot 6H_2O$, 99.9%), diethylene glycol (DEG, 99%), and sodium bromide (NaBr, 99.99%) were purchased from Alfa Aesar. Rhodium(II) trifluoroacetate dimer [$Rh_2(COOCF_3)_4$, 98%], sodium tetrachloropalladate (II) [Na_2PdCl_4, 99.99%], sodium trifluoroacetate ($NaCOOCF_3$, 98%), and triethylene glycol (TREG, >99%) were purchased from Sigma-Aldrich. Ethylene glycol (EG, >99%) was purchased from J. T. Baker. Poly(vinylpyrrolidone) (PVP), with an average molecular weight of 40 000, was purchased from TCI. Solvents, including acetone, ethanol, and hexanes, were of analytical grade. All chemicals were used as received.

Synthesis. The heat-up syntheses of Rh icosahedra, cubes, and triangular plates from molecular precursors were based on our previously reported procedure.[11] The Rh reagent (0.1 mmol by Rh atom) and PVP stabilizer (2 mmol by repeating unit) were dissolved in 10 mL of polyol solvent using a sonic bath or, in the case of higher-order solvents, a 65 °C water bath. For the synthesis of Rh icosahedra, $NaCOOCF_3$ [8:1 ratio with $Rh_2(COOCF_3)_4$] was also added. The solution was stirred vigorously with a magnetic stir bar under bubbling argon in a 25 mL three-neck flask fitted with a condenser and septum. Temperature was maintained using a digital controller with glass-coated thermocouple (Gemini, J-KEM Scientific) and 25 mL heating mantle (Glas-Col). The solution was heated to a temperature at which particle nucleation began, as evidenced by a darkening of the color. After holding at these conditions for 15 min, the solution was heated to a focusing temperature, causing the solution color to darken further, and maintained there for 75 min before being quenched with a cold water bath. For aliquot studies, a portion of the reaction was removed with a syringe through the septum.

For the synthesis of PVP and Cl-capped Rh clusters, 0.6 mmol of $RhCl_3 \cdot xH_2O$ and 12 mmol of PVP were dissolved in 60 mL of TREG using a 65 °C water bath followed by sonic bath. The reaction solution was then pipetted into a 100 mL three-neck flask equipped with a condenser, thermometer, and septum, and also containing a magnetic stir bar. The reaction solution was bubbled with Ar from a needle inserted through the septum and the temperature was increased to 100 °C. This temperature was maintained for 75 min, resulting in the color of the solution darkening from orange to brown as Rh clusters formed, before quenching the reaction with a cold water bath.

For the cluster-mediated synthesis of Rh cubes, 0.9 mmol of NaBr was dissolved in 10 mL of Rh clusters in TREG (3:1 Br^-:Cl^-) using a sonic bath before being transferred into the reaction setup and heated to 140 °C for 75 min. For the cluster-mediated synthesis of Rh icosahedra, 3.6 mmol of $NaCOOCF_3$ was dissolved in 10 mL of Rh clusters in TREG (12:1 $COOCF_3^-$:Cl^-) using a sonic bath before being transferred into the reaction setup and heated to 125 °C for 75 min. For the cluster-mediated synthesis of Rh triangular plates, 10 mL of Rh clusters in TREG was transferred into the reaction setup and heated to 135 °C for 75 min. All reactions were quenched with a cold water bath

when completed. For aliquot studies, the scale of the reaction was increased to 30 mL of Rh clusters and portions of the reaction were removed with a syringe through the septum.

Spherical and cubic Pt particles were synthesized by dissolving 0.1 mmol $H_2PtCl_6 \cdot 6H_2O$ and PVP stabilizer (2 mmol by repeating unit) in EG, the latter with 1 mmol NaBr additionally added, and heating to 175 °C for 75 min. Spherical Pd particles were synthesized by dissolving 0.1 mmol Na_2PdCl_4 and PVP in EG and then heating to 95 °C for 75 min. Once at room temperature, all reaction solutions were diluted by adding three times the volume of 2:1 acetone:hexanes. All Rh, Pt, and Pd particles were separated from polyol solvents and excess reagents by centrifugation at 10 000 rpm for 3 min and redispersed in ethanol with a sonic bath. Excess hexanes were added and the particles were separated twice more by centrifugation at 5000 rpm for 3 min before being stored dispersed in ethanol.

Characterization. Transmission electron microscopy (TEM) images were obtained from a JEOL 1200 EX II microscope operating at an accelerating voltage of 80 kV. High-resolution TEM (HRTEM) and high-angle annular dark field scanning TEM (HAADF-STEM) images were collected using a JEOL 2010F field emission microscope, operating at an accelerating voltage of 200 kV. All microscopy samples were prepared by casting one drop of dispersed sample in ethanol onto a 400-mesh Formvar and carbon-coated copper grid (Electron Microscopy Sciences). Lattice spacings and crystallographic structure were determined from the fast Fourier transform (FFT) of the HRTEM images, using Gatan Digital Micrograph software. Particle counting analysis used a minimum of 200 individual particles and size was determined using the ImageJ program (http://rsbweb.nih.gov/ij/). Powder X-ray diffraction (XRD) data were collected on a Bruker Advance D8 X-ray diffractometer using Cu Kα radiation. UV−visible (UV−vis) absorption spectra were obtained using an Ocean Optics HR4000 spectrometer with a DH-2000-BAL light source and quartz cuvettes. X-ray photoelectron spectroscopy (XPS) analyses were performed on a monochromatic Al Kα source Kratos Axis Ultra operating at 14 kV and 20 mA for an X-ray power of 280 W. Spectra were collected with a photoelectron takeoff angle of 90° from the sample surface plane and were referenced to the C_{1s} peak with a binding energy of 284.5 eV. Inductively coupled plasma atomic emission spectroscopy (ICP-AES) was performed on a Perkin-Elmer Optima 5300DV using synthetic standards from High Purity Standards to calibrate the results. Prior to ICP-AES analysis, samples were digested in a 3.5% *aqua regia* solution. Small-angle X-ray scattering (SAXS) measurements were performed on a Molecular Metrology pinhole camera system. The source was operated at 45 kV and 0.67 mA while the sample to detector distance was 0.5 m. After correcting for the background, the data was analyzed using Irena software.[74]

Conflict of Interest: The authors declare no competing financial interest.

Supporting Information Available: XPS and SAXS characterization of Rh clusters, TEM images of aliquots taken during the formation of Pt and Pd nanoparticles, and additional characterization (TEM, HRTEM, HAADF-STEM, and UV−vis absorption spectroscopy) of the formation of Rh nanoparticles. This material is available free of charge *via* the Internet at http://pubs.acs.org.

Acknowledgment. This work was supported by funds from The Pennsylvania State University and the U.S. National Science Foundation (DMR-1305564). Electron microscopy was performed at the Penn State Microscopy and Cytometry Facility (University Park, PA) and at the Materials Characterization Lab of the Penn State Materials Research Institute. The authors thank Trevor Clark, Joseph Kulik, Xiaojun Weng, Ke Wang, Henry Gong, Raegan Johnson, Jennifer Gray, and Vincent Bojan for their assistance with characterization and helpful discussions.

REFERENCES AND NOTES

1. Roduner, E. Size Matters: Why Nanomaterials are Different. *Chem. Soc. Rev.* **2006**, *35*, 583–592.
2. Popczun, E. J.; McKone, J. R.; Read, C. G.; Biacchi, A. J.; Wiltrout, A. M.; Lewis, N. S.; Schaak, R. E. Nanostructured Nickel Phosphide as an Electrocatalyst for the Hydrogen Evolution Reaction. *J. Am. Chem. Soc.* **2013**, *135*, 9267–9270.
3. Murray, C. B.; Kagan, C. R.; Bawendi, M. G. Synthesis and Characterization of Monodisperse Nanocrystals and Close-Packed Nanocrystal Assemblies. *Annu. Rev. Mater. Sci.* **2000**, *30*, 545–610.
4. Scholl, J. A.; Koh, A. L.; Dionne, J. A. Quantum Plasmon Resonances of Individual Metallic Nanoparticles. *Nature* **2012**, *483*, 421–427.
5. Gao, M.-R.; Zhang, S.-R.; Xu, Y.-F.; Zheng, Y.-R.; Jiang, J.; Yu, S.-H. Self-Assembled Platinum Nanochain Networks Driven by Induced Magnetic Dipoles. *Adv. Funct. Mater.* **2014**, *24*, 916–924.
6. Biacchi, A. J.; Vaughn, D. D., II; Schaak, R. E. Synthesis and Crystallographic Analysis of Shape-Controlled SnS Nanocrystal Photocatalysts: Evidence for a Pseudotetragonal Structural Modification. *J. Am. Chem. Soc.* **2013**, *135*, 11634–11644.
7. Xia, Y.; Xiong, Y.; Lim, B.; Skrabalak, S. E. Shape-Controlled Synthesis of Metal Nanocrystals: Simple Chemistry Meets Complex Physics? *Angew. Chem., Int. Ed.* **2009**, *48*, 60–103.
8. Xia, X.; Zeng, J.; Oetjen, L. K.; Li, Q.; Xia, Y. Quantitative Analysis of the Role Played by Poly(vinylpyrrolidone) in Seed-Mediated Growth of Ag Nanocrystals. *J. Am. Chem. Soc.* **2012**, *134*, 1793–1801.
9. Ortiz, N.; Skrabalak, S. E. On the Dual Roles of Ligands in the Synthesis of Colloidal Metal Nanostructures. *Langmuir* **2014**, *30*, 6649–6659.
10. Lim, B.; Wang, J.; Camargo, P. H. C.; Cobley, C. M.; Kim, M. J.; Xia, Y. Twin-Induced Growth of Palladium−Platinum Alloy Nanocrystals. *Angew. Chem., Int. Ed.* **2009**, *48*, 6304–6308.
11. Biacchi, A. J.; Schaak, R. E. The Solvent Matters: Kinetic *versus* Thermodynamic Shape Control in the Polyol Synthesis of Rhodium Nanoparticles. *ACS Nano* **2011**, *5*, 8089–8099.
12. Humphrey, S. M.; Grass, M. E.; Habas, S. E.; Niesz, K.; Somorjai, G. A.; Tilley, T. D. Rhodium Nanoparticles from Cluster Seeds: Control of Size and Shape by Precursor Addition Rate. *Nano Lett.* **2007**, *7*, 785–790.
13. Xie, S.; Peng, H.-C.; Lu, N.; Wang, J.; Kim, M. J.; Xie, Z.; Xia, Y. Confining the Nucleation and Overgrowth of Rh to the {111} Facets of Pd Nanocrystal Seeds: The Roles of Capping Agent and Surface Diffusion. *J. Am. Chem. Soc.* **2013**, *135*, 16658–16667.
14. O'Brien, M. N.; Jones, M. R.; Brown, K. A.; Mirkin, C. A. Universal Noble Metal Nanoparticle Seeds Realized through Iterative Reductive Growth and Oxidative Dissolution Reactions. *J. Am. Chem. Soc.* **2014**, *136*, 7603–7606.
15. DeSantis, C. J.; Skrabalak, S. E. Core Values: Elucidating the Role of Seed Structure in the Synthesis of Symmetrically Branched Nanocrystals. *J. Am. Chem. Soc.* **2013**, *135*, 10–13.
16. Lin, M.; Fu, Z. Y.; Tan, H. R.; Tan, J. P. Y.; Ng, S. C.; Teo, E. Hydrothermal Synthesis of CeO_2 Nanocrystals: Ostwald Ripening or Oriented Attachment? *Cryst. Growth Des.* **2012**, *12*, 3296–3303.
17. LaMer, V. K. Nucleation in Phase Transitions. *Ind. Eng. Chem.* **1952**, *44*, 1270–1277.
18. Sugimoto, T. Preparation of Monodispersed Colloidal Particles. *Adv. Colloid Interface Sci.* **1987**, *28*, 65–108.
19. Lifshitz, I. M.; Slyozov, V. V. The Kinetics of Precipitation from Supersaturated Solid Solutions. *J. Phys. Chem. Solids* **1961**, *19*, 35–50.
20. Auer, S.; Frenkel, D. Prediction of Absolute Crystal-Nucleation Rate in Hard-Sphere Colloids. *Nature* **2001**, *409*, 1020–1023.
21. Gasser, U.; Weeks, E. R.; Schofield, A.; Pusey, P. N.; Weitz, D. A. Real-Space Imaging of Nucleation and Growth in Colloidal Crystallization. *Science* **2001**, *292*, 258–262.
22. Ostwald, W. Studien uber die Bildung und Umwandlung Fester Korper. *Z. Phys. Chem.* **1897**, *22*, 289–330.
23. Peng, X.; Wickham, J.; Alivisatos, A. P. Kinetics of II-VI and III-V Colloidal Semiconductor Nanocrystal Growth: "Focusing"

of Size Distributions. *J. Am. Chem. Soc.* **1998**, *120*, 5343–5344.
24. Schilling, T.; Schope, H. J.; Oettel, M.; Opletal, G.; Snook, I. Precursor-Mediated Crystallization Process in Suspensions of Hard Spheres. *Phys. Rev. Lett.* **2010**, *105*, 025701.
25. Tan, P.; Xu, N.; Xu, L. Visualizing Kinetic Pathways of Homogeneous Nucleation in Colloidal Crystallization. *Nat. Phys.* **2014**, *10*, 73–79.
26. Gebauer, D.; Volkel, A.; Colfen, H. Stable Prenucleation Calcium Carbonate Clusters. *Science* **2008**, *322*, 1819–1822.
27. Baumgartner, J.; Dey, A.; Bomans, P. H. H.; Le Coadou, C. c.; Fratzl, P.; Sommerdijk, N. A. J. M.; Faivre, D. Nucleation and Growth of Magnetite from Solution. *Nat. Mater.* **2013**, *12*, 310–314.
28. Chai, J.; Liao, X.; Giam, L. R.; Mirkin, C. A. Nanoreactors for Studying Single Nanoparticle Coarsening. *J. Am. Chem. Soc.* **2012**, *134*, 158–161.
29. Ustarroz, J.; Altantzis, T.; Hammons, J. A.; Hubin, A.; Bals, S.; Terryn, H. The Role of Nanocluster Aggregation, Coalescence, and Recrystallization in the Electrochemical Deposition of Platinum Nanostructures. *Chem. Mater.* **2014**, *26*, 2396–2406.
30. Xie, J.; Yan, C.; Zhang, Y.; Gu, N. Shape Evolution of "Multibranched" Mn-Zn Ferrite Nanostructures with High Performance: A Transformation of Nanocrystals into Nanoclusters. *Chem. Mater.* **2013**, *25*, 3702–3709.
31. Qian, H.; Zhu, Y.; Jin, R. Atomically Precise Gold Nanocrystal Molecules with Surface Plasmon Resonance. *Proc. Natl. Acad. Sci., U.S.A.* **2012**, *109*, 696–700.
32. Schmid, G. Metal Clusters and Cluster Metals. *Polyhedron* **1988**, *7*, 2321–2329.
33. Kumara, C.; Zuo, X.; Ilavsky, J.; Chapman, K. W.; Cullen, D. A.; Dass, A. Super-Stable, Highly Monodisperse Plasmonic Faradaurate-500 Nanocrystals with 500 Gold Atoms: $Au_{\sim 500}(SR)_{\sim 120}$. *J. Am. Chem. Soc.* **2014**, *136*, 7410–7417.
34. Tsunoyama, H.; Tsukuda, T. Magic Numbers of Gold Clusters Stabilized by PVP. *J. Am. Chem. Soc.* **2009**, *131*, 18216–18217.
35. Kim, B. H.; Hackett, M. J.; Park, J.; Hyeon, T. Synthesis, Characterization, and Application of Ultrasmall Nanoparticles. *Chem. Mater.* **2014**, *26*, 59–71.
36. Penn, R. L.; Banfield, J. F. Imperfect Oriented Attachment: Dislocation Generation in Defect-Free Nanocrystals. *Science* **1998**, *281*, 969–971.
37. Banfield, J. F.; Welch, S. A.; Zhang, H.; Ebert, T. T.; Penn, R. L. Aggregation-Based Crystal Growth and Microstructure Development in Natural Iron Oxyhydroxide Biomineralization Products. *Science* **2000**, *289*, 751–754.
38. Cho, K.-S.; Talapin, D. V.; Gaschler, W.; Murray, C. B. Designing PbSe Nanowires and Nanorings through Oriented Attachment of Nanoparticles. *J. Am. Chem. Soc.* **2005**, *127*, 7140–7147.
39. Schliehe, C.; Juarez, B. H.; Pelletier, M.; Jander, S.; Greshnykh, D.; Nagel, M.; Meyer, A.; Foerster, S.; Kornowski, A.; Klinke, C.; et al. Ultrathin PbS Sheets by Two-Dimensional Oriented Attachment. *Science* **2010**, *329*, 550–553.
40. Li, D.; Nielsen, M. H.; Lee, J. R. I.; Frandsen, C.; Banfield, J. F.; De Yoreo, J. J. Direction-Specific Interactions Control Crystal Growth by Oriented Attachment. *Science* **2012**, *336*, 1014–1018.
41. Bisson, L.; Boissiere, C.; Nicole, L.; Grosso, D.; Jolivet, J. P.; Thomazeau, C. c.; Uzio, D.; Berhault, G.; Sanchez, C. Formation of Palladium Nanostructures in a Seed-Mediated Synthesis through an Oriented-Attachment-Directed Aggregation. *Chem. Mater.* **2009**, *21*, 2668–2678.
42. Zheng, H.; Smith, R. K.; Jun, Y.-w.; Kisielowski, C.; Dahmen, U.; Alivisatos, A. P. Observation of Single Colloidal Platinum Nanocrystal Growth Trajectories. *Science* **2009**, *324*, 1309–1312.
43. Yuk, J. M.; Park, J.; Ercius, P.; Kim, K.; Hellebusch, D. J.; Crommie, M. F.; Lee, J. Y.; Zettl, A.; Alivisatos, A. P. High-Resolution EM of Colloidal Nanocrystal Growth Using Graphene Liquid Cells. *Science* **2012**, *336*, 61–64.
44. Liao, H.-G.; Cui, L.; Whitelam, S.; Zheng, H. Real-Time Imaging of Pt_3Fe Nanorod Growth in Solution. *Science* **2012**, *336*, 1011–1014.
45. Polte, J.; Ahner, T. T.; Delissen, F.; Sokolov, S.; Emmerling, F.; Thunemann, A. F.; Kraehnert, R. Mechanism of Gold Nanoparticle Formation in the Classical Citrate Synthesis Method Derived from Coupled *in Situ* XANES and SAXS Evaluation. *J. Am. Chem. Soc.* **2010**, *132*, 1296–1301.
46. Wuithschick, M.; Paul, B.; Bienert, R.; Sarfraz, A.; Vainio, U.; Sztucki, M.; Kraehnert, R.; Strasser, P.; Rademann, K.; Emmerling, F.; et al. Size-Controlled Synthesis of Colloidal Silver Nanoparticles Based on Mechanistic Understanding. *Chem. Mater.* **2013**, *25*, 4679–4689.
47. Sathiyanarayanan, R.; Alimohammadi, M.; Zhou, Y.; Fichthorn, K. A. Role of Solvent in the Shape-Controlled Synthesis of Anisotropic Colloidal Nanostructures. *J. Phys. Chem. C* **2011**, *115*, 18983–18990.
48. Raju, M.; van Duin, A. C. T.; Fichthorn, K. A. Mechanisms of Oriented Attachment of TiO_2 Nanocrystals in Vacuum and Humid Environments: Reactive Molecular Dynamics. *Nano Lett.* **2014**, *14*, 1836–1842.
49. Xie, S.; Lu, N.; Xie, Z.; Wang, J.; Kim, M. J.; Xia, Y. Synthesis of Pd-Rh Core−Frame Concave Nanocubes and Their Conversion to Rh Cubic Nanoframes by Selective Etching of the Pd Cores. *Angew. Chem., Int. Ed.* **2012**, *51*, 10266–10270.
50. Yuan, Y.; Yan, N.; Dyson, P. J. Advances in the Rational Design of Rhodium Nanoparticle Catalysts: Control *via* Manipulation of the Nanoparticle Core and Stabilizer. *ACS Catal.* **2012**, *2*, 1057–1069.
51. Park, K. H.; Jang, K.; Kim, H. J.; Son, S. U. Near-Monodisperse Tetrahedral Rhodium Nanoparticles on Charcoal: The Shape-Dependent Catalytic Hydrogenation of Arenes. *Angew. Chem., Int. Ed.* **2007**, *46*, 1152–1155.
52. Sneed, B. T.; Kuo, C.-H.; Brodsky, C. N.; Tsung, C.-K. Iodide-Mediated Control of Rhodium Epitaxial Growth on Well-Defined Noble Metal Nanocrystals: Synthesis, Characterization, and Structure-Dependent Catalytic Properties. *J. Am. Chem. Soc.* **2012**, *134*, 18417–18426.
53. Kanuru, V. K.; Humphrey, S. M.; Kyffin, J. M. W.; Jefferson, D. A.; Burton, J. W.; Armbruster, M.; Lambert, R. M. Evidence for Heterogeneous Sonogashira Coupling of Phenylacetylene and Iodobenzene Catalyzed by Well Defined Rhodium Nanoparticles. *Dalton Trans.* **2009**, 7602–7605.
54. Borodko, Y.; Lee, H. S.; Joo, S. H.; Zhang, Y.; Somorjai, G. Spectroscopic Study of the Thermal Degradation of PVP-Capped Rh and Pt Nanoparticles in H_2 and O_2 Environments. *J. Phys. Chem. C* **2009**, *114*, 1117–1126.
55. Saito, Y. Wulff Polyhedra Derived from Morse Potentials and Crystal Habits of bcc and fcc Metal Particles. *J. Cryst. Growth* **1981**, *53*, 273–279.
56. Akita, T.; Kohyama, M.; Haruta, M. Electron Microscopy Study of Gold Nanoparticles Deposited on Transition Metal Oxides. *Acc. Chem. Res.* **2013**, *46*, 1773–1782.
57. Herzing, A. A.; Kiely, C. J.; Carley, A. F.; Landon, P.; Hutchings, G. J. Identification of Active Gold Nanoclusters on Iron Oxide Supports for CO Oxidation. *Science* **2008**, *321*, 1331–1335.
58. Duarte, R. B.; Krumeich, F.; van Bokhoven, J. A. Structure, Activity, and Stability of Atomically Dispersed Rh in Methane Steam Reforming. *ACS Catal.* **2014**, *4*, 1279–1286.
59. Bohren, C. F.; Huffman, D. R. *Absorption and Scattering of Light by Small Particles*; John Wiley & Sons, Inc.: New York, 1983.
60. Skrabalak, S. E.; Wiley, B. J.; Kim, M.; Formo, E. V.; Xia, Y. On the Polyol Synthesis of Silver Nanostructures: Glycolaldehyde as a Reducing Agent. *Nano Lett.* **2008**, *8*, 2077–2081.
61. Fievet, F.; Lagier, J. P.; Figlarz, M. Preparing Monodisperse Metal Powers in Micrometer and Submicrometer Sizes by the Polyol Process. *MRS Bull.* **1989**, *14*, 29–34.
62. Bock, C.; Paquet, C.; Couillard, M.; Botton, G. A.; MacDougall, B. R. Size-Selected Synthesis of PtRu Nano-Catalysts: Reaction and Size Control Mechanism. *J. Am. Chem. Soc.* **2004**, *126*, 8028–8037.
63. Chang, S. C.; Ho, Y.; Weaver, M. J. Applications of Real-Time FTIR Spectroscopy to the Elucidation of Complex Electroorganic Pathways: Electrooxidation of Ethylene Glycol on

Gold, Platinum, and Nickel in Alkaline Solution. *J. Am. Chem. Soc.* **1991**, *113*, 9506–9513.
64. Malola, S.; Lehtovaara, L.; Enkovaara, J.; Hakkinen, H. Birth of the Localized Surface Plasmon Resonance in Monolayer-Protected Gold Nanoclusters. *ACS Nano* **2014**, *7*, 10263–10270.
65. Millstone, J. E.; Wei, W.; Jones, M. R.; Yoo, H.; Mirkin, C. A. Iodide Ions Control Seed-Mediated Growth of Anisotropic Gold Nanoparticles. *Nano Lett.* **2008**, *8*, 2526–2529.
66. Penn, R. L.; Soltis, J. A. Characterizing Crystal Growth by Oriented Aggregation. *CrystEngComm* **2014**, *16*, 1409–1418.
67. Zhang, Y.; Grass, M. E.; Kuhn, J. N.; Tao, F.; Habas, S. E.; Huang, W.; Yang, P.; Somorjai, G. A. Highly Selective Synthesis of Catalytically Active Monodisperse Rhodium Nanocubes. *J. Am. Chem. Soc.* **2008**, *130*, 5868–5869.
68. Wulff, G. On the Question of Speed of Growth and Dissolution of Crystal Surfaces. *Z. Krystallogr. Mineral.* **1901**, *34*, 449–530.
69. Reyes-Gasga, J.; Tehuacanero-Nunez, S.; Montejano-Carrizales, J. M.; Gao, X.; Jose-Yacaman, M. Analysis of the Contrast in Icosahedral Gold Nanoparticles. *Top. Catal.* **2007**, *46*, 23–30.
70. Scarabelli, L.; Coronado-Puchau, M.; Giner-Casares, J. J.; Langer, J.; Liz-Marzan, L. M. Monodisperse Gold Nanotriangles: Size Control, Large-Scale Self-Assembly, and Performance in Surface-Enhanced Raman Scattering. *ACS Nano* **2014**, *8*, 5833–5842.
71. Xiong, Y.; McLellan, J. M.; Chen, J.; Yin, Y.; Li, Z.-Y.; Xia, Y. Kinetically Controlled Synthesis of Triangular and Hexagonal Nanoplates of Palladium and Their SPR/SERS Properties. *J. Am. Chem. Soc.* **2005**, *127*, 17118–17127.
72. Elechiguerra, J. L.; Reyes-Gasga, J.; Yacaman, M. J. The Role of Twinning in Shape Evolution of Anisotropic Noble Metal Nanostructures. *J. Mater. Chem.* **2006**, *16*, 3906–3919.
73. Personick, M. L.; Langille, M. R.; Zhang, J.; Harris, N.; Schatz, G. C.; Mirkin, C. A. Synthesis and Isolation of {110}-Faceted Gold Bipyramids and Rhombic Dodecahedra. *J. Am. Chem. Soc.* **2011**, *133*, 6170–6173.
74. Ilavsky, J.; Jemian, P. R. *Irena*: Tool Suite for Modeling and Analysis of Small-Angle Scattering. *J. Appl. Crystallogr.* **2009**, *42*, 347–353.